Intermetallics 136 (2021) 107267

Contents lists available at ScienceDirect

Intermetallics

journal homepage: www.elsevier.com/locate/intermet

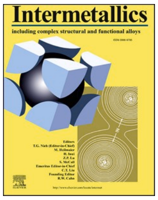

General route to fabricate ultrafine metallic glass powders directly from their own crystalline states by localized pulsed electrical discharge atomization

Lei Zuo[a], Xuan Li[b], Kai Zhang[a], Tao Zhang[b],*

[a] School of Aerospace Engineering, Beijing Institute of Technology, Beijing, 100081, China
[b] Key Laboratory of Aerospace Materials and Performance (Ministry of Education), School of Materials Science and Engineering, Beihang University, Beijing, 100191, China

A R T I C L E I N F O

Keywords:
Metallic glasses
Glass transition and crystallization
Microstructure
Finite-element modeling

A B S T R A C T

Localized pulsed electrical discharge (PED) atomization is developed as a general route to fabricate ultrafine metallic glass powders with high purity and sphericity, which cannot be achieved by conventional techniques, like mechanical alloying, chemical reduction and water/gas atomization. The new atomization process starts with a localized melting on crystalline alloy surface by PED. During the melting process, multiple crystalline phases in the starting alloy are melted and then homogenized to form a uniform melted zone. Finally, the melted zone is atomized to produce ultrafine powders under the explosive force. The obtained particle size is mainly in the range of 1–10 μm. The results also show that it is easier to vitrify the produced powders for alloys with higher glass-forming ability (GFA). However, considering that the cooling rates achieved by PED atomization and melt-spinning technique are comparable, the GFA of the starting alloy will not play a determining role in the formation of glassy powders as long as it can guarantee the formation of glassy ribbons by melt-spinning technique. In this case, the ratio of melted zone size to crystalline phase size become the determining factor. The amorphization degree and compositional homogeneity can be improved by refining the starting alloy with low GFA. Besides, the experimental and simulation results both eliminate the possible Mo pollution from the tool electrode. This work will hopefully expand the applications of metallic glasses.

1. Introduction

Metallic glasses have attracted considerable attention over the past three decades due to their amorphous nature and unique physical, mechanical and chemical properties [1–10]. As one important form, metallic glass powders have advantages in many fields like catalysis, magnetic powder core, 3D printing, etc [11–17]. At present, methods for producing metallic glass powders mainly includes mechanical alloying, chemical reduction and water/gas atomization. For mechanical alloying, it is an effective process to produce metallic glass powders at room temperature by ball milling [18–20]. However, there are several shortcomings for mechanical alloying, such as time-consuming, contamination coming from ball milling media and containers, and irregular shapes with sharp protrusions and corners. For chemical reduction, it is a facile method to fabricate metallic glass nanoparticles [14,16,21–25]. But this method is limited to B-doped and P-doped systems. For water/gas atomization, it is the most commonly used method to fabricate glassy powders for various alloy systems [12,20,26–29]. The particle size of the powders fabricated by water/gas atomization normally ranges from several tens of micrometers to hundreds of micrometers. It can be seen that the particle size is large. Normally, high water/gas pressure is needed to refine particle size. Nevertheless, it is still uneasy to fabricate powders with diameters below 20 μm by water/gas atomization technique [12,20,26–29]. For water atomization method, it also faces a problem of unsatisfactory particle sphericity. Therefore, it can be drawn that the present techniques for producing metallic glass powder cannot provide a general route to synthesize ultrafine metallic glass powders with high purity and sphericity, and it is meaningful to seek a new method.

Compared to mechanical alloying and chemical reduction, atomization is more suitable to be applied as a universal method to fabricate metallic glass powders with high purity and sphericity. The main

---

* Corresponding author.
E-mail address: zhangtao@buaa.edu.cn (T. Zhang).

https://doi.org/10.1016/j.intermet.2021.107267
Received 13 October 2020; Received in revised form 7 June 2021; Accepted 10 June 2021

limitation of atomization method is that the obtained particle size is relatively large. Analyzed from the principle of atomization, there are two ways to reduce the particle size, i.e., to limit the size of the melting zone and increase the external force of atomization. During conventional atomization process, the whole starting alloy is melted. However, if the melting is localized to a small zone on the crystalline starting alloy surface and the atomization of the melted zone is in an explosive way, finer powders can be synthesized. This idea can be realized by pulsed electrical discharge (PED). Actually, the phenomenon of PED has been widely utilized in electrical discharge machining, which is a non-conventional machining process based on a thermo-electrical material removal mechanism [30]. The machining is achieved by generating a succession of controlled electrical discharges between the tool electrode and the workpiece immersed in a dielectric fluid. Each of those discharges removes a small amount of material due to the extremely high temperatures formed in the vicinity of the plasma channel generated during the discharge process. According to its principle, PED has a potential to become a universal route to synthesize ultrafine metallic glass powders in various alloy systems. Similar to water/gas atomization technique, the new method is called localized PED atomization.

Considering that the atomized particles should be expelled easily and quickly from the gap between electrodes, a “wire” type is preferred for localized PED atomization (Fig. 1(a)). This type of localized PED atomization uses a wire electrode as the tool electrode. During atomization process, the wire electrode moves at a high speed that it can easily carry the atomized particles out the gap. Normally, the wire electrode is made of materials with high melting temperature like Mo, W, etc. The yields can be readily increased by using multiple parallel wire electrodes. It also should be noted that this type has no strict requirements on the shape of the starting alloy.

In this paper, localized PED atomization in the “wire” type was conducted on Zr-, Ti- and Fe-based crystalline alloys in order to fabricate corresponding metallic glass powders. Effects of GFA and crystalline phase size of the starting alloy on the glass formation and the compositional homogeneity of the atomized particles were studied by experimental studies and finite element simulation. The possible pollution from the wire electrode was also evaluated and discussed. Furthermore, a model for the localized PED atomization process was established.

2. Experimental

Alloy ingots with nominal compositions of $Zr_{55}Al_{10}Ni_5Cu_{30}$, $Ti_{45.5}Zr_{6.5}Cu_{39.9}Ni_{5.1}Sn_2Si_1$, $Fe_{36}Ni_{36}B_{19.2}Si_{4.8}Nb_4$, $Fe_{72}B_{17}Si_5Mo_6$ and $Fe_{72}B_{23}Si_5$ (at.%) were prepared by arc-melting the mixture of the pure elements as well as an industry-grade FeB alloy on a Cu hearth in a Ti gettered Ar atmosphere. All ingots weigh about 30 g. Besides, $Fe_{36}Ni_{36}B_{19.2}Si_{4.8}Nb_4$ plates of 2 mm-thick were fabricated by Cu mold injection. In order to produce fully $Fe_{36}Ni_{36}B_{19.2}Si_{4.8}Nb_4$ glassy ribbons, the $Fe_{36}Ni_{36}B_{19.2}Si_{4.8}Nb_4$ ingots were re-melted using high-frequency induction, and the melt was spun on a rotating Cu wheel (20 cm in diameter) at 4000 rpm in pure Ar atmosphere by the single-roller melt-spinning technique. The critical diameters (D_c) of these alloys are summarized in Table 1. To guarantee the compositional homogeneity, the ingots were re-melted at least 5 times. The ingots were first cut into square rods of 8 × 8 × 15 mm by a DK7716 type wire electrical discharge machine. Localized PED atomization was performed by machining the square rods along their longitudinal direction using the wire electrical discharge machine, as shown in Fig. 1(a). There are four electrical parameters that can be altered in the PED atomization process, as illustrated in Fig. 1(b). In this work, the discharge voltage $V = 90$ V, discharge current $I = 1.5$ A, pulse duration $t_{on} = 24$ μs and pulse interval

Table 1
Critical diameters (D_c) and glass transition temperatures (T_g) of the Zr-, Ti- and Fe-based metallic glasses.

Alloy (at.%)	T_g	D_c (mm)	Ref.
$Zr_{55}Al_{10}Ni_5Cu_{30}$	685	10	[31]
$Ti_{45.5}Zr_{6.5}Cu_{39.9}Ni_{5.1}Sn_2Si_1$	670	4	[32]
$Fe_{36}Ni_{36}B_{19.2}Si_{4.8}Nb_4$	763	2	This work
$Fe_{72}B_{17}Si_5Mo_6$	794	1	[33]
$Fe_{72}B_{23}Si_5$	\	<1	[33]

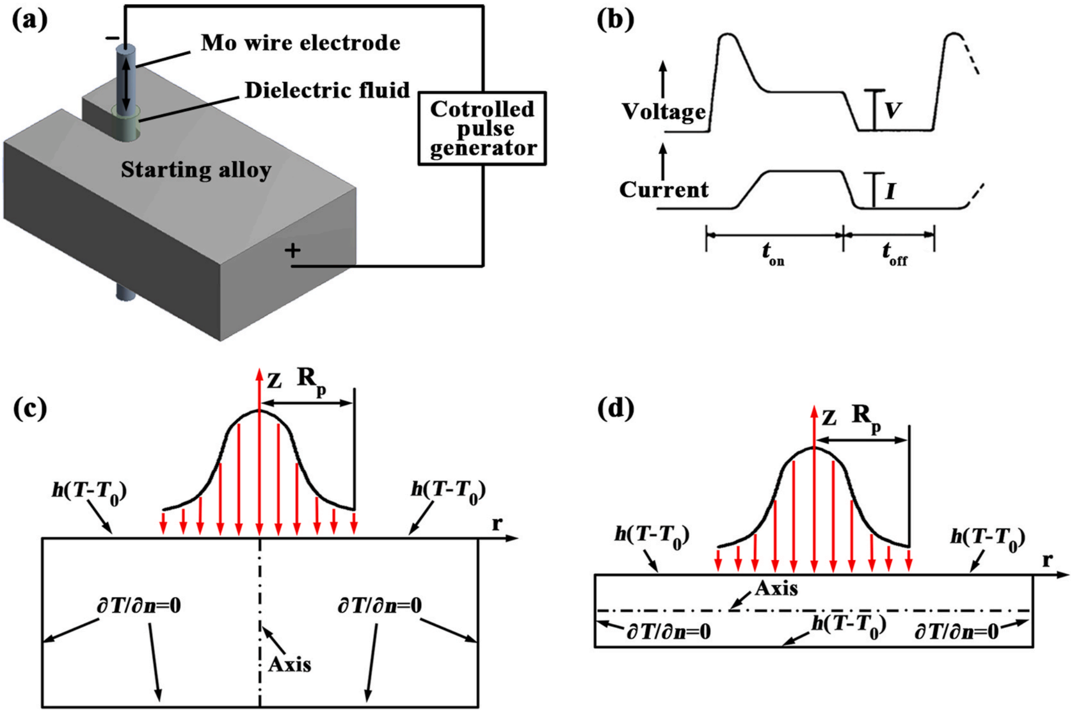

Fig. 1. (a) Schematic diagram of the localized PED atomization. (b) Actual profile of a single pulse. Boundary conditions of finite element analysis for (c) the starting alloy and (d) the Mo wire electrode.

$t_{off} = 5$ μs. The wire tool electrode is Mo wire with a diameter of ~120 μm. Structures of the prepared powders and the treated alloys were examined by X-ray diffraction (XRD, Bruker D8-advance) with Co-Kα radiation, scanning electron microscopy (SEM, JEOL JSM-7500F) coupled with an energy-dispersive spectrometer (EDS). Thermal properties were investigated by differential scanning calorimetry (DSC, NETZSCH STA 449F3) and Hot Disk TPS 2500.

Finite element analysis on the PED atomization process for the $Fe_{36}Ni_{36}B_{19.2}Si_{4.8}Nb_4$ starting alloy was performed on ANSYS WORKBENCH 19.0 software. Transient thermal was chosen as the analysis system. Due to that the finite element model is axisymmetric for the starting alloy, only a quarter model was built in order to reduce the amount of calculation (Fig. S1). The finite element models were created with medium mesh. Because the thermal load located in and near the discharge channel is large and concentrated, the mesh is finer in this part. We optimize the element size by gradually reducing it until further mesh refinement will not obviously change the temperature field at the end of an electrical discharge. The applied boundary conditions for the starting alloy and Mo wire are illustrated in Fig. 1(c) and (d), respectively. The material properties of the starting alloy and Mo wire are summarized in Table 2. For the starting alloy, the density (ρ) was determined by Archimede's method. The melting temperature (T_m), liquidus temperature (T_l), specific heat (c) and latent heat of fusion (L_m) was measured by DSC (Figs. S2–S3). The thermal conductivity (κ) was measured by Hot Disk TPS 2500 (Fig. S4). The ambient temperature is set to be 300 K. In order to simplify the complicated situation, some assumptions are made during the modeling as follows [34]: (1) The model is developed for a single electrical discharge; (2) The shape of the elements is not affected by thermal expansion; (3) Conduction is considered as the mode of heat transfer to the electrodes; (4) The work domain is axisymmetric about the Z axis for the starting alloy; (5) Starting alloy and Mo wire electrode are homogeneous and isotropic in nature. In order to acquire a more accurate result, heat flux with Gaussian distribution is adopted. The adopted heat flux $Q(r)$ for starting alloy is given by [34]:

$$Q(r) = \frac{4.57FVI}{\pi R_p^{\,2}} e^{-4.5\left(\frac{r^2}{R_p^{\,2}}\right)} \tag{1}$$

where F is the percentage of energy absorbed by the starting alloy (anode, F_a) or the Mo wire electrode (cathode, F_c), V (V) is the discharge voltage, and I (A) is the discharge current. In this work, $F_a = 10\%$ [35], $F_c = 12\%$ [35], $V = 90$ V and $I = 1.5$ A. R_p (m) is the radius of the plasma channel. R_p does not remain constant during discharge but grows with time. R_p depends on various parameters such as electrode material, pulse current, pulse duration, and polarity. In this work, a semi-empirical equation (Eq. (2)) proposed by Ikai and Hashiguchi is used as an effective relation for the modeling of the growth of the plasma channel with time t (s) [36]:

$$R_p = 2.04 \times 10^{-3} I^{0.43} t^{0.44} \tag{2}$$

The correctness of the finite element modeling is mainly guaranteed by that the adopted models, boundary conditions and equations (including the constants that put in) have been used in other similar simulation works and the simulation results agrees well with the experimental studies [34–36].

Table 2
Density (ρ), melting temperature (T_m), liquidus temperature (T_l), thermal conductivity (κ), specific heat (c) and latent heat of fusion (L_m) of the $Fe_{36}Ni_{36}B_{19.2}Si_{4.8}Nb_4$ starting alloy and Mo wire used for finite element analysis.

Material	ρ (g cm^{-2})	T_m (K)	T_l (K)	κ (W m^{-1} K^{-1})	c (J kg^{-1} K^{-1})	L_m (J/kg)	Ref.
Starting alloy	7.70	1267	1372	31	474	1.6E5	This work
Mo wire	10.22	2896	\	138	276	2.9E5	[37]

3. Results

Localized PED atomization was performed on Zr-, Ti- and Fe-based crystalline alloys fabricated by arc-melting. The processing parameters, like discharge voltage, discharge current, pulse duration and pulse interval, were selected based on our previous study [38]. Because this work aims to study the influence of material characteristics on properties of atomized particles, and the fundamental characteristics of PED atomization, we did not study the effects of processing parameters on properties of atomized particles. It does not mean that processing parameters are not important. On the contrary, according to our previous study [38], these parameters should have important effects on glass formation of atomized particles. The synthesized particles were collected and analyzed by XRD (Fig. 2). Only broad diffraction peaks typical for amorphous structure are detected in the XRD pattern of Zr- and Ti-based powders, indicating that these particles are amorphous. For the XRD pattern of the $Fe_{36}Ni_{36}B_{19.2}Si_{4.8}Nb_4$ powder, only small peaks are superimposed on a broad diffraction peak, indicating that it consists of mainly amorphous phases and a small amount of nano-crystalline phase. In the XRD patterns of $Fe_{72}B_{17}Si_5Mo_6$ and $Fe_{72}B_{23}Si_5$ powders, broad diffraction peaks are also seen with more intensified crystalline peaks. It should be noted that partly vitrification occurs even for the $Fe_{72}B_{23}Si_5$ starting alloy with a very low GFA that can only form glassy ribbons by melt-spinning technique, which suggests that the new atomization method can generate a very high cooling rate for the atomized powder. Due to that the $Fe_{36}Ni_{36}B_{19.2}Si_{4.8}Nb_4$ powder mainly consists of amorphous phase with only a small amount of nano-crystalline phase, this composition is more helpful to analyze the influence factors in glass formation of atomized powders. Thus, the composition of $Fe_{36}Ni_{36}B_{19.2}Si_{4.8}Nb_4$ was selected for further analysis.

The PED treatment is localized to a small zone (in micrometer scale) on crystalline alloy and the size of the melted zone is also in micrometer scale. It is reasonable to consider the situation that some crystalline phases in the starting alloy are larger than the melted zone. In that case, it is unlikely to obtain glassy powders by PED atomization and the atomized powders may show a great fluctuation in composition.

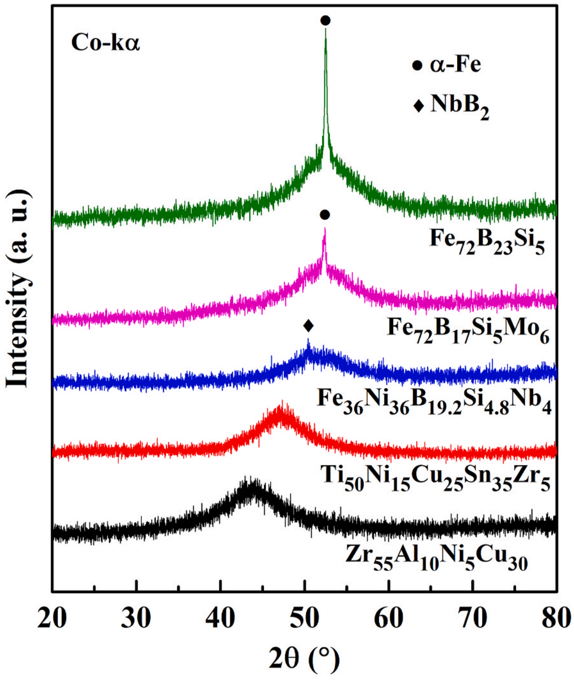

Fig. 2. XRD patterns of Zr-, Ti- and Fe-based metallic glass powders.

Therefore, it is meaningful to study the effects of crystalline phase size on the formation of glassy powders. In this study, the phase size of the arc-melted $Fe_{36}Ni_{36}B_{19.2}Si_{4.8}Nb_4$ alloy was decreased by rapid solidification. Specifically, 2 mm-thick plates with smaller crystalline phases were fabricated by Cu mold casting. It is obvious that the rapid solidified plate has a finer microstructure and the arc-melted ingot has a coarser one. Thus, for simplicity, the arc-melted ingot is denoted as the "coarse" one and the rapid solidified plate as the "fine" one. Fig. 3(a) and (b) show the back-scattered electron (BSE) images of the cross-sections of the "coarse" and "fine" starting alloys after PED treatment, respectively. It can be seen that the crystalline phases in the "fine" starting alloy are obviously smaller than that in the "coarse" one. It also can be seen that a homogenized layer is formed on the surface of the "fine" starting alloy while the homogenized layer is not clear for the "coarse" starting alloy. Besides, Fig. 3(a) and (b) show that the PED treatment will not lead to a detectable growth of the crystalline phases in the heat affected zone but only refine the surface layer, which means that it will not deteriorate the glass formation when the PED treated surface is involved in the next atomization process. The powders derived from the "coarse" and "fine" starting alloys are shown in Fig. 3(c) and (d), respectively. It can be found that the two powders both show a very high sphericity.

The particle size distributions of the two powders synthesized from the "coarse" and "fine" starting alloys are displayed in Fig. 4(a). For both of them, the particle sizes mainly lie in the range from 1 to 10 μm. Considering the statistical error, it is believed that crystalline phase size of starting alloy shows no evident effects on particle size distribution of atomized powder. However, the crystalline phase size does influence the glass formation of the synthesized powder. As indicated by the DSC curves (Fig. 4(b)), compared to the glassy ribbons, the glass transition temperature T_g and initial crystallization temperature T_x of the atomized powders shift to lower values and the shift for the powder fabricated from the "coarse" starting alloy is larger. The lower values of T_g and T_x mean a reduction of thermal stability of the glassy phase. The content of glassy phase in the atomized powder is estimated by assuming that the melt-spun ribbons are fully amorphous and that the content of the glassy phase has a linear relationship with the crystallization enthalpy. The contents of the glassy phase for powders fabricated from the "coarse" and "fine" starting alloys are calculated to be 77% and 97%, respectively. It shows that the content of glassy phase increases with the reduction of crystalline phase size in the starting alloy. For the "fine" starting alloy, the atomized powder is nearly fully amorphous. In addition, the crystallization peaks for the atomized powders are broader than that for the glassy ribbons, which may be due to that the composition of the glassy phase in the atomized powders is not uniform to some extent. Thus, the compositional fluctuation in different particles was further analyzed (Fig. 4(c)). Twenty particles are randomly selected each for the two powders obtained from the "coarse" and "fine" starting alloy. In the EDS analysis, element B is neglected for that EDS show no capability of detecting it. The mean values and standard deviations for different elements are summarized in Table 3. It shows that the mean values are approximately the same for the two powders obtained from the "coarse" and "fine" starting alloys. Besides, it can be seen that the composition shows certain fluctuation in different particles for both the powders synthesized from the "coarse" and "fine" starting alloys. However, the fluctuation in composition for the powder fabricated from the "fine" starting alloy is greatly smoothed compared to that for the powder obtained from the "coarse" starting alloy. It can be concluded that a smaller crystalline phase size is beneficial to glass formation and compositional homogeneity for atomized particles. Furthermore, no Mo element is detected in the atomized powders, which eliminates the pollution from Mo wire electrode and thus the atomized powders have a high purity.

In order to acquire a better understanding of the basic questions involved in the localized PED atomization process, finite element analysis was performed (Fig. 5). At the end of an electrical discharge, the highest temperatures reach 8880 K and 3472 K for the $Fe_{36}Ni_{36}B_{19.2}Si_{4.8}Nb_4$ starting alloy and Mo wire electrode, respectively. The extremely high temperature of 8880 K is the source of explosive

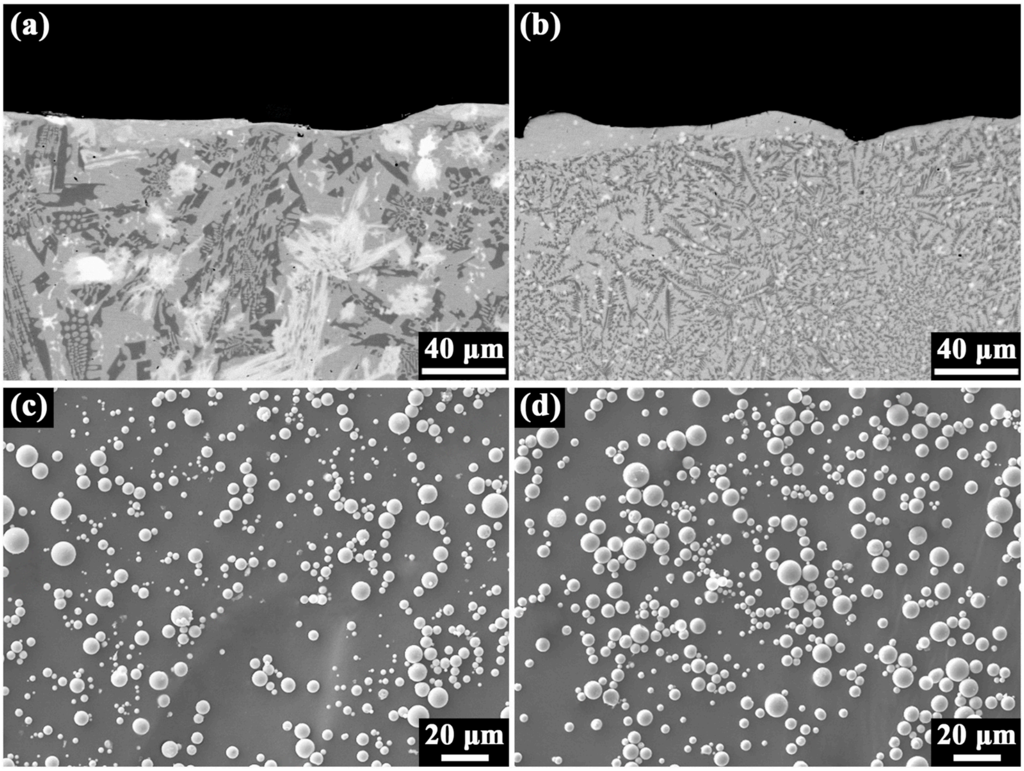

Fig. 3. BSE images of the cross-sections of the (a) "coarse" and (b) "fine" $Fe_{36}Ni_{36}B_{19.2}Si_{4.8}Nb_4$ starting alloys after PED treatment. SEM images of the powders synthesized from the (c) "coarse" and (d) "fine" $Fe_{36}Ni_{36}B_{19.2}Si_{4.8}Nb_4$ starting alloys.

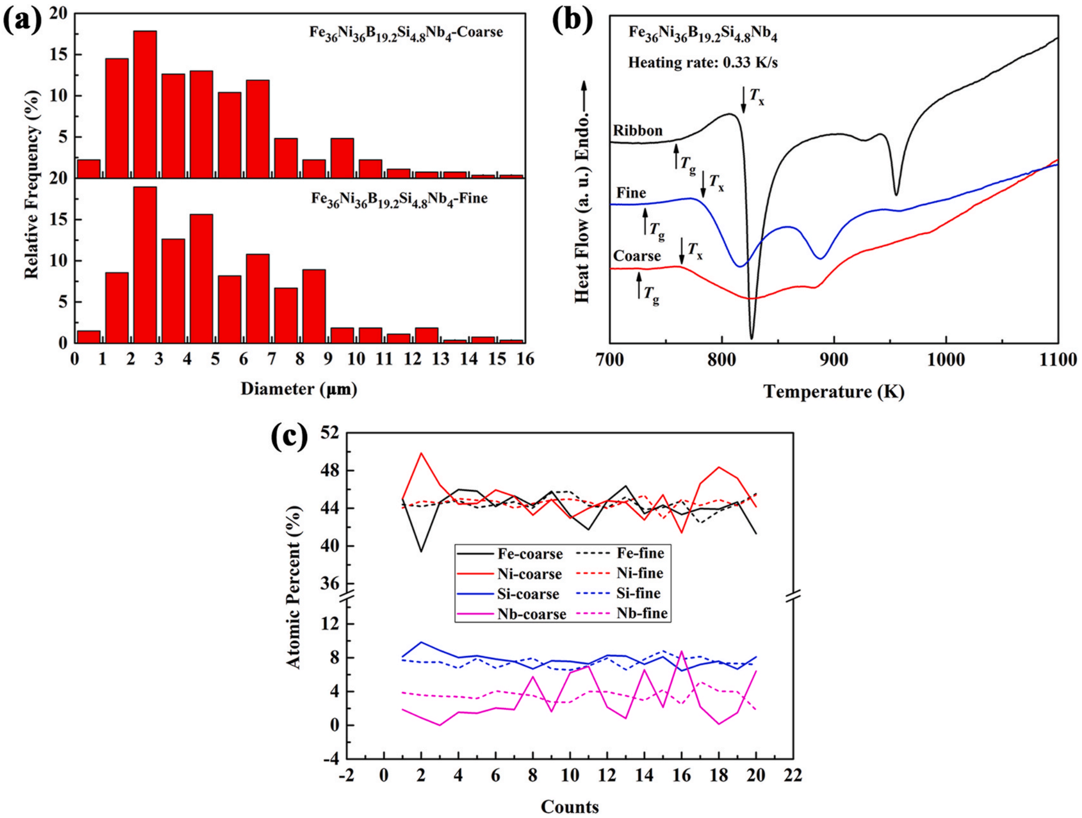

Fig. 4. (a) Particle size distributions of the synthesized powders. (b) DSC curves of the atomized powders and the glassy ribbons. (c) Statistical analysis of the compositional fluctuation for the atomized $Fe_{36}Ni_{36}B_{19.2}Si_{4.8}Nb_4$ powders.

Table 3
Statistical analysis of the compositional fluctuations for the powders synthesized from the “coarse” and “fine” $Fe_{36}Ni_{36}B_{19.2}Si_{4.8}Nb_4$ starting alloy.

	Coarse				Fine			
	Fe	Ni	Si	Nb	Fe	Ni	Si	Nb
Mean value	44.07	45.10	7.78	3.05	44.44	44.59	7.45	3.52
Standard deviation	1.70	1.96	0.79	2.64	0.77	0.57	0.60	0.74

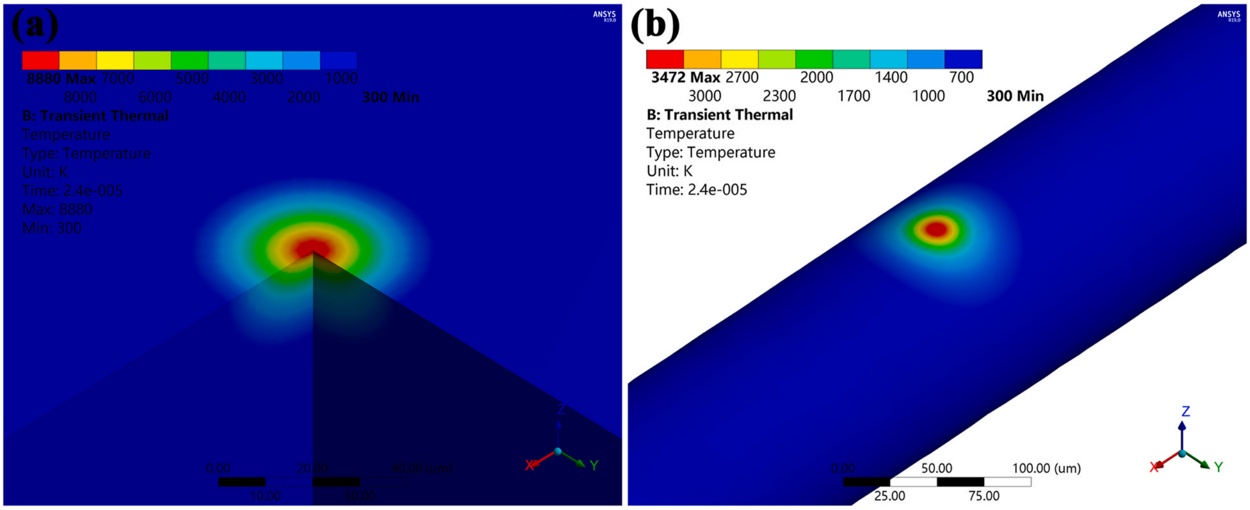

Fig. 5. Temperature field of the PED treated (a) $Fe_{36}Ni_{36}B_{19.2}Si_{4.8}Nb_4$ starting alloy and (b) Mo wire electrode.

atomization for the starting alloy, which will be further discussed below. It can be seen that the temperature of the PED treated starting alloy is much higher than that of the treated Mo wire electrode. The much lower temperature in the melted zone for the treated Mo wire means a smaller force that can atomize the melted zone, partly explaining the no detection of Mo element in the synthesized powders.

The two-dimensional isotherms (liquidus temperature for the starting alloy and melting temperature for the Mo wire) are illustrated in Fig. 6(a). According to the isotherms, the melted zone size can be calculated. For the starting alloy, the diameter and depth of the melted zone is 40.17 and 15.32 μm, respectively. For the Mo wire, the diameter and depth of the melted zone is 13.19 and 1.88 μm, respectively. The melted zone for the Mo wire is estimated to be less than 1.5% of that for the starting alloy. Thus, the pollution from Mo wire electrode will not be distinct even if Mo pollution does exist. On the other hand, the melted zone size will limit the size of the atomized particle, which may explain why particles with diameters above 20 μm are rarely seen. Calculated by the mean diameter of ~5 μm, one melted zone will generate about 100 particles. Besides, it can be seen that the melted zone size is comparable to the size of the Nb-rich phase (the white phase shown in Fig. 3(a)) in the "coarse" starting alloy. Thus, it is possible for plasma channel to focus only on the Nb-rich phase. In that case, Nb-rich particles are obtained and it is unlikely for these Nb-rich particles to form glassy structure due to low GFA. However, for the "fine" starting alloy, the chance for plasma channel to focus only on one phase is greatly reduced, and thus the composition of the atomized powders is more homogeneous and the glass formation for the atomized powders is improved from 77% to 97%.

As we all know, cooling rate has an important role in the glass formation. Thus, the cooling behaviors of the PED treated starting alloy and the atomized particles with different diameters are analyzed (Fig. 6(b)). By assuming that the melted zone is not atomized to particles for the $Fe_{36}Ni_{36}B_{19.2}Si_{4.8}Nb_4$ starting alloy, the cooling of the point with the highest temperature at the end of an electrical discharge is recorded (Fig. 6(b)). Its cooling rate in the temperature range from T_g to T_l is as high as 2.63×10^7 K/s. This high cooling rate can explain the glassy layer formed on the starting alloy surface [38]. The cooling rates for the atomized particles with diameters of 2.5, 5, 10 and 20 μm are 4.10×10^6, 2.16×10^6, 1.09×10^6 and 5.49×10^5 K/s, respectively. These cooling rates are comparable to that achieved by the melt-spinning technique (the cooling rate of melt-spinning technique is in the order of 10^3–10^6 K/s [39]). Therefore, these cooling rates are high enough to fully vitrify atomized particles as long as these particles have GFA that can guarantee the formation of glassy ribbons by melt-spinning technique.

4. Discussion

Based on the XRD results displayed in Fig. 2, it can be seen that fully amorphous powders can be directly fabricated from arc-melted starting alloys with relatively high GFA by localized PED atomization technique. For arc-melted starting alloys with relatively low GFA ($D_c \leq 2$ mm), only partly vitrification of atomized powders can be fulfilled by the new atomization method. However, our results also show that glass formation in atomized powders can be improved by refining crystalline phases for starting alloys with low GFA. Thus, the new atomization method is also applicable for producing metallic glass powders with low GFA on condition that the crystalline phases in the starting alloys are fine enough. In that sense, as one of its advantages, PED atomization process has a potential to become a general method to fabricate glassy powders with high purity and sphericity in various alloy systems (not limited to alloy systems with high GFA), which cannot be achieved by conventional techniques.

According to the thermo-electrical material removal mechanism of electrical discharge machining [30,40], a model for the localized PED atomization process is proposed based on the single electrical discharge (Fig. 7). For the present technique used for localized PED atomization (Fig. 1(a)), the pollution from the Mo wire electrode is undetectable due to that the PED treated Mo wire electrode has a lower temperature (39%) and a smaller melted zone (1.5%) than the starting alloy. Thus, the atomization process of Mo wire electrode is not displayed in the proposed model for the PED atomization process. When the distance between the starting alloy and the Mo wire electrode is reduced to a certain value, a breakdown of water occurs and a plasma channel is formed (Fig. 7(a)). Once the plasma channel is formed, the total pulse energy will be transferred to the water, starting alloy and the Mo wire electrode along this channel. At first, the channel expands at a speed of several hundred meters per second, and later is reduced to several tens of meters per second due to the inertia of water. The channel will be tapered as a result of the magnetic compression effect caused by the increase in the channel current and the thermal compression effect caused by the cooling of water. The channel maintains a small cross-sectional dimension under the dual action of expansion and compression (Fig. 7(b)), which makes the plasma channel have an extremely high temperature (in the order of 10^4 K) and a very high pressure (transient pressure can reach tens or even hundreds of atmospheres). The channel with high temperature and high pressure strongly heats a small zone on the starting alloy surface, and the metal in the small zone is heated to become superheated metal (indicated in red shown in Fig. 7(a)–(c)). Due to the heating of the plasma channel, a gas bubble containing metal vapor is also formed around the plasma channel (Fig. 7(b)). As the channel expands and its pressure drops rapidly, it is possible that a small amount of superheated metal is explosively

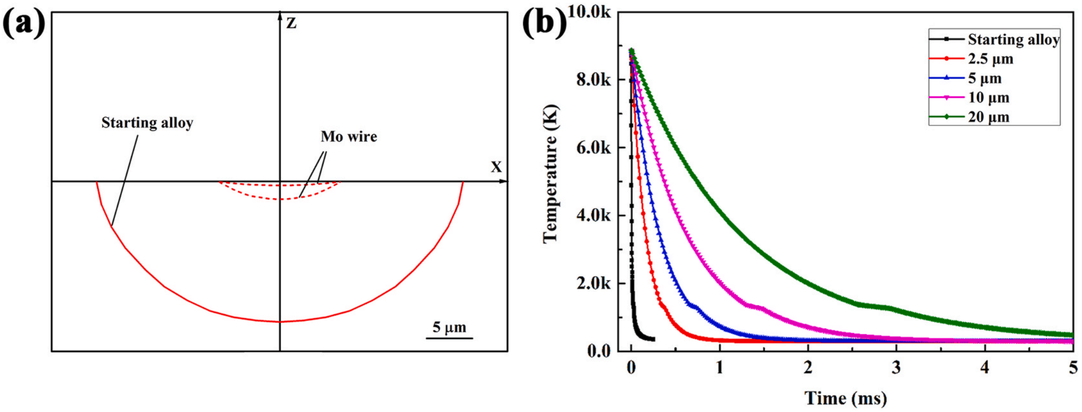

Fig. 6. (a) The melted zone sizes for the PED treated $Fe_{36}Ni_{36}B_{19.2}Si_{4.8}Nb_4$ starting alloy and Mo wire electrode. (b) The cooling curves of the PED treated $Fe_{36}Ni_{36}B_{19.2}Si_{4.8}Nb_4$ starting alloy and the atomized powders with diameters of 2.5, 5, 10 and 20 μm.

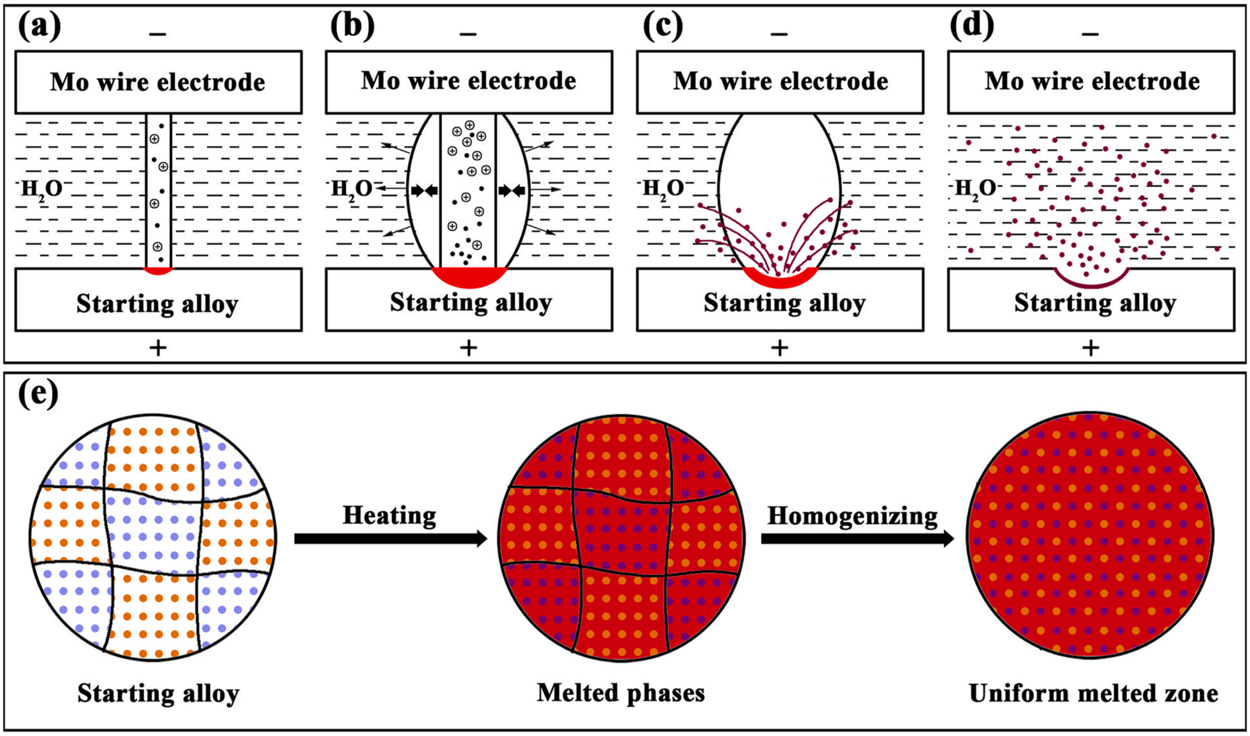

Fig. 7. Schematic illustration of the localized PED atomization process. (a) Formation of plasma channel. (b) Expansion and stabilization of plasma channel. (c) Collapse of channel and explosive evaporation of the superheated molten metal. (d) Rupture of bubble and formation of particles. (e) Microstructural evolution of the starting alloy during the atomization process.

vaporized, and a small amount of metal is thrown out under the action of the explosive force. However, the thrown out of the metal mainly occurs in the form of liquid phase after the end of the current pulse [40]. As shown in Fig. 7(c), at the end of the current pulse, the channel quickly contracts and collapses. At this time, the number of charged particles is rapidly reduced, which is a process called deionization. The bubble continues to expand to the maximum size and then shrinks. The pressure inside the bubble is rapidly lowered to near atmospheric pressure, which leads to the evaporation of the superheated molten metal at a low pressure. Meanwhile, the molten metal is also thrown out together to form a pit on the surface of the starting alloy. The bubble ruptures when it shrinks to a certain extent, and the entire PED atomization process ends (Fig. 7(d)). Finally, ultrafine particles are synthesized by suspending in water. Due to the rapid cooling rate, an amorphous layer may also be formed on the starting alloy surface (Fig. 7(d)).

Along with the localized PED atomization process, the microstructure of the starting alloy evolves (Fig. 7(e)). Normally, crystalline starting alloys with high GFA consist of multiple phases. In the ideal case, the melted zone generated by the heating of the plasma channel contains a large number of crystalline phases. During the atomization process, these phases are melted and then are homogenized to form a uniform melted zone. The driving force for homogenization comes from the reduction of chemical potential and the explosive force resulting from the violent evaporation of the molten metal.

During the PED atomization process, there are so many factors that may affect the formation of glassy powders that it is unrealistic to analyze the influences of each one. Thus, we mainly consider two pairs of contradictory factors as follows:

i. GFA vs. cooling rate

According to the XRD patterns shown in Fig. 2, it may be concluded subconsciously that GFA of starting alloy is a determining factor for glass formation in the atomized powders. However, based on the finite element analysis, the cooling rate for the atomized powder is in the order of 10^5–10^6 K/s, which is comparable to the cooling rate achieved by the melt-spinning method. The high cooling rate of the PED atomization can also be demonstrated by the partly vitrification of the particles fabricated from the $Fe_{72}B_{23}Si_5$ starting alloy with a very low GFA ($D_c < 1$ mm) that can only form glassy ribbons. Thus, it is reasonable to conclude that the GFA of the starting alloy is not the determining factor in the formation of glassy powders as long as the starting alloy has a GFA that can guarantee the formation of glassy ribbons by melt-spinning technique. It should be noted that it does not mean the GFA of the starting alloy is not an important factor. In fact, the GFA may indirectly affect the glass formation for the atomized powders by influencing the phase type, phase size, etc., in the crystalline starting alloy.

ii. Crystalline phase size vs. melted zone size

Different from water/gas atomization process that the whole starting alloy is melted, PED atomization is localized to a small zone on crystalline starting alloy surface (in micrometer scale). The melted zone is relatively small that the effects of the crystalline phase size of the starting alloy on the glass formation of the atomized powders cannot be neglected. According to our study, the diameter of the melted zone for the $Fe_{36}Ni_{36}B_{19.2}Si_{4.8}Nb_4$ starting alloy is calculated to be about 40 μm, and the depth to be about 15 μm. If the size of one phase in the starting alloy exceeds the depth or even the diameter of the melted zone, the melted zone may be localized only on the phase. As a result, it is not feasible to obtain powders with the target composition and the GFA of the atomized powders may be decreased greatly. In order to verify this assumption, we devised two alloys with different crystalline phase sizes achieved by different cooling rates. The DSC curves (Fig. 4(b)) show that the powder fabricated from the “fine” starting alloys has a higher content of amorphous phase than that from the “coarse” alloy. Besides, the EDS analysis (Fig. 4(c)) shows that the compositions of the atomized particles show certain fluctuations around the mean compositions and the powder fabricated from the "fine" starting alloy show a smaller fluctuation in composition than that from the "coarse" one. These results demonstrate that the crystalline phase size of the starting alloy plays a crucial role in the glass formation and the compositional homogeneity of the atomized powders. Actually, a sufficient homogenization of the melted zone is also of great importance in the glass formation and the compositional homogeneity of the atomized powders. As illustrated in Fig. 7(e), the melted zone is homogenized due to the reduction of chemical potential and the explosive force that atomize the melted zone to particles. At present, it is difficult to measure the magnitude of the explosive force. However, considering that the explosive force is high enough to atomize a small melted zone with a diameter of about 40 μm to about 100 particles, the force is assumed to be large enough to fully homogenize the melted zone. It can be concluded that the ratio of melted zone size to crystalline phase size is a crucial and determining factor in the formation of glassy powders by localized PED atomization method when the starting alloy has a GFA that can guarantee the formation of glassy ribbons by melt-spinning technique. It is apparent that a large value of the ratio for the starting alloy is more desirable for a better formation of glassy powders. The crystalline phases in the starting alloys can be downscaled by rapid solidification method, while the melted zone size can be enlarged by adjusting the electrical parameters used in the localized PED atomization process.

5. Conclusions

Localized PED atomization is successfully applied to synthesize ultrafine Zr-, Ti- and Fe-based metallic glass powders directly from their own crystalline states. The influence of material characteristics on the properties of the atomized particles and the fundamental characteristics of the PED atomization method were systematically studied based on experimental and simulation studies. The main conclusions are summarized as follows:

(1) The synthesized $Fe_{36}Ni_{36}B_{19.2}Si_{4.8}Nb_4$ powder possesses very high sphericity. Most particles show diameters below 10 μm. Due to that PED treated Mo wire electrode has a lower temperature (39%) and a smaller melted zone (1.5%) than the starting alloy, the pollution from the Mo wire electrode is not detected and thus the synthesized powders have a high purity.

(2) In general, the amorphization degree of the synthesized powder increases with the increase of GFA. However, due to the comparable cooling rates achieved by localized PED atomization and melt-spinning technique, the GFA of the starting alloy will not be the determining factor that affects the glass formation of the atomized powders when the GFA of the starting alloy can guarantee the formation of glassy ribbons by melt-spinning technique. In this case, the ratio of melted zone size to crystalline phase size for the starting alloy is the real determining factor. It is a feasible method to improve the glass formation and compositional homogeneity for the atomized powder with low GFA by refining the starting alloy.

(3) A model for the localized PED atomization process is established. In the model, the atomization proceeds as follows: (i) formation of plasma channel, (ii) expansion and stabilization of plasma channel, (iii) collapse of channel and explosive evaporation of the superheated molten metal and (iv) rupture of bubble and formation of particles. During the atomization process, multiple crystalline phases in the starting alloy are melted and then homogenized to form a uniform melted zone due to the violent evaporation of the molten metal.

CRediT authorship contribution statement

Lei Zuo: Conceptualization, Methodology, Finite Element Simulation, Data curation, Writing – original draft. **Xuan Li:** Performing Experiments. **Kai Zhang:** Methodology, Supervision. **Tao Zhang:** Conceptualization, Writing – review & editing, Supervision.

Declaration of competing interest

The authors declare that they have no known competing financial interests or personal relationships that could have appeared to influence the work reported in this paper.

Acknowledgments

This work was supported by the China Postdoctoral Science Foundation (grant Nos. 2020M680014 and 2019M652566), the National Key Research and Development Program of China (grant No. 2016YFB0300500), the National Natural Science Foundation of China (grant Nos. 51971006 and 51571005).

Appendix A. Supplementary data

Supplementary data to this article can be found online at https://doi.org/10.1016/j.intermet.2021.107267.

References

[1] C.C. Yu, J.P. Chu, H.L. Jia, Y.L. Shen, Y.F. Gao, P.K. Liaw, Y. Yokoyama, Influence of thin-film metallic glass coating on fatigue behavior of bulk metallic glass: experiments and finite element modeling, Mater. Sci. Eng., A 692 (2017) 146–155.
[2] T. Zhang, A. Inoue, T. Masumoto, Amorphous Zr-Al-TM (TM= Co, Ni, Cu) alloys with significant supercooled liquid region of over 100 K, Mater. Trans., JIM 32 (1991) 1005–1010.
[3] B. Sarac, J. Schroers, Designing tensile ductility in metallic glasses, Nat. Commun. 4 (2013) 2158.
[4] J.L. Gu, Y. Shao, L.X. Shi, J.J. Si, K.F. Yao, Novel corrosion behaviours of the annealing and cryogenic thermal cycling treated Ti-based metallic glasses, Intermetallics 110 (2019) 106467.
[5] C.A. Schuh, T.C. Hufnagel, U. Ramamurty, Mechanical behavior of amorphous alloys, Acta Mater. 55 (2007) 4067–4109.
[6] M. Ashby, A. Greer, Metallic glasses as structural materials, Scripta Mater. 54 (2006) 321–326.
[7] W.H. Zhou, Y.H. Meng, F.H. Duan, W. Huang, J.H. Yao, J. Pan, Y.X. Wang, Y. Li, The effect of oxygen on phase formation in an industrial Zr based bulk metallic glass, Intermetallics 129 (2021) 107055.
[8] J. Pan, Y.P. Ivanov, W.H. Zhou, Y. Li, A.L. Greer, Strain-hardening and suppression of shear-banding in rejuvenated bulk metallic glass, Nature 578 (2020) 559–562.
[9] M.M. Khan, A. Nemati, Z.U. Rahman, U.H. Shah, H. Asgar, W. Haider, Recent advancements in bulk metallic glasses and their applications: a review, Crit. Rev. Solid State Mater. Sci. 43 (2018) 233–268.
[10] L.H. Liu, C. Yang, Y.G. Yao, F. Wang, W.W. Zhang, Y. Long, Y.Y. Li, Densification mechanism of Ti-based metallic glass powders during spark plasma sintering process, Intermetallics 66 (2015) 1–7.
[11] J.Q. Wang, Y.H. Liu, M.W. Chen, G.Q. Xie, D.V. Louzguine-Luzgin, A. Inoue, J. H. Perepezko, Rapid degradation of azo dye by Fe-based metallic glass powder, Adv. Funct. Mater. 22 (2012) 2567–2570.
[12] Y. Liu, S. Niu, F. Li, Y.T. Zhu, Y.H. He, Preparation of amorphous Fe-based magnetic powder by water atomization, Powder Technol. 213 (2011) 36–40.
[13] E. Williams, N. Lavery, Laser processing of bulk metallic glass: a review, J. Mater. Process. Technol. 247 (2017) 73–91.
[14] Q.T. Phan, K.C. Poon, H. Sato, A review on amorphous noble-metal-based electrocatalysts for fuel cells: synthesis, characterization, performance, and future perspective, Int. J. Hydrogen Energy 46 (2021) 14190–14211.
[15] P.C. Zhang, C. Zhang, D. Ouyang, L. Liu, Enhancement of plasticity and toughness of 3D printed binary $Zr_{50}Cu_{50}$ bulk metallic glass composite by deformation-induced martensitic transformation, Scripta Mater. 192 (2021) 7–12.
[16] Y.W. Bai, X.F. Bian, J.Y. Qin, X.X. Li, K.K. Song, The relationship between structures and magnetic properties of Fe-B amorphous nanoparticles, J. Non-Cryst. Solids 528 (2020) 119723.
[17] Y.Z. Lu, S. Su, S.B. Zhang, Y.J. Huang, Z.X. Qin, X. Lu, W. Chen, Controllable additive manufacturing of gradient bulk metallic glass composite with high strength and tensile ductility, Acta Mater. 206 (2021) 116632.
[18] X. Liu, X. Wang, Y. Si, X. Zhong, F. Han, Crystallization behavior of $Al_{70}Fe_{12.5}V_{12.5}Nb_5$ amorphous alloy formed by mechanical alloying, Materials 12 (2019) 383.
[19] M. Sherif El-Eskandarany, L.A. Al-Hajji, A. Al-Hazza, Fabrication of new metallic glassy $Ti_{40.6}Cu_{15.4}Ni_{8.5}Al_{5.5}W_{30}$ alloy powders by mechanical alloying and subsequent SPS consolidation, Adv. Powder Technol. 28 (2017) 814–819.
[20] T.C. Zhao, C.G. Chen, X.J. Wu, C.Z. Zhang, A.A. Volinsky, J.J. Hao, FeSiBCrC amorphous magnetic powder fabricated by gas-water combined atomization, J. Alloys Compd. 857 (2021) 157991.

[21] Y.S. Yang, L.Z. Zhuang, R.J. Lin, M.R. Li, X.Y. Xu, T.E. Rufford, Z.H. Zhu, A facile method to synthesize boron-doped Ni/Fe alloy nano-chains as electrocatalyst for water oxidation, J. Power Sources 349 (2017) 68–74.

[22] Y. Kang, J. Henzie, H. Gu, J. Na, A. Fatehmulla, B.S.A. Shamsan, A.M. Aldhafiri, W. A. Farooq, Y. Bando, T. Asahi, B. Jiang, H. Li, Y. Yamauchi, Mesoporous metal-metalloid amorphous alloys: the first synthesis of open 3D mesoporous Ni-B amorphous alloy spheres via a dual chemical reduction method, Small 16 (2020), e1906707.

[23] Y. Kang, B. Jiang, J. Yang, Z. Wan, J. Na, Q. Li, H. Li, J. Henzie, Y. Sakka, Y. Yamauchi, T. Asahi, Amorphous alloy architectures in pore walls: mesoporous amorphous NiCoB alloy spheres with controlled compositions via a chemical reduction, ACS Nano (2020) 17224–17232.

[24] M.T. Kiani, C.M. Barr, S. Xu, D. Doan, Z. Wang, A. Parakh, K. Hattar, X.W. Gu, Ductile metallic glass nanoparticles via colloidal synthesis, Nano Lett. 20 (2020) 6481–6487.

[25] L. Gao, K. Liu, L.Y. Zhang, Z.W. Xin, Y.J. Yang, G.T. Wei, T.T. Yuan, Microwave-assisted catalytic transfer hydrogenation of fatty acid methyl esters using metal-doped nickel-boride-cetyltrimethylammonium bromide amorphous alloy catalyst, Int. J. Energy Res. (2021) 1–19.

[26] H. Han, P.F. Wang, Y.J. Li, R.H. Liu, C. Tian, Effect of water supply pressure on atomization characteristics and dust-reduction efficiency of internal mixing air atomizing nozzle, Adv. Powder Technol. 31 (2020) 252–268.

[27] K. Kassym, A. Perveen, Atomization processes of metal powders for 3D printing, Mater. Today: Proceedings 26 (2020) 1727–1733.

[28] M.W. Wei, S.Y. Chen, M. Sun, J. Liang, C.S. Liu, M. Wang, Atomization simulation and preparation of 24CrNiMoY alloy steel powder using VIGA technology at high gas pressure, Powder Technol. 367 (2020) 724–739.

[29] Z.X. Chang, W.X. Wang, Y.Q. Ge, J. Zhou, P. Dong, Z.Q. Cui, Micro-mechanical properties and corrosion resistance of $Zr_{55}Cu_{30}Al_{10}Ni_5$ bulk metallic glass fabricated by spark plasma sintering, J. Alloys Compd. 780 (2019) 220–227.

[30] B. Izquierdo, S. Plaza, J.A. Sánchez, I. Pombo, N. Ortega, Numerical prediction of heat affected layer in the EDM of aeronautical alloys, Appl. Surf. Sci. 259 (2012) 780–790.

[31] J. Luo, H.P. Duan, C.L. Ma, S.J. Pang, T. Zhang, Effects of yttrium and erbium additions on glass forming ability and mechanical properties of bulk glassy Zr-Al-Ni-Cu Alloys, Mater. Trans. 47 (2006) 450–453.

[32] E.H. Yin, S.J. Pang, X.D. Hui, M. Zhang, L.C. Zhuo, C. Chen, T. Zhang, Correlation of glass-forming ability to thermal properties in Ti-based bulk metallic glasses, J. Alloys Compd. 546 (2013) 7–13.

[33] X. Li, Z.G. Shi, T. Zhang, Effect of similar element substitution on Fe-B-Si-Mo bulk metallic glasses studied by experiment and ab initio molecular dynamics simulation, J. Alloys Compd. 784 (2019) 1139–1144.

[34] M. Hosseini Kalajahi, S. Rash Ahmadi, S. Nadimi Bavil Oliaei, Experimental and finite element analysis of EDM process and investigation of material removal rate by response surface methodology, Int. J. Adv. Manuf. Technol. 69 (2013) 687–704.

[35] H. Singh, Experimental study of distribution of energy during EDM process for utilization in thermal models, Int. J. Heat Mass Tran. 55 (2012) 5053–5064.

[36] T. Ikai, I. Fujita, K. Hashiguchi, Heat input radius for crater formation in the electric discharge machining, IEEE Trans. Ind. Appl. 112 (1992) 943–949.

[37] P. Allen, X.L. Chen, Process simulation of micro electro-discharge machining on molybdenum, J. Mater. Process. Technol. 186 (2007) 346–355.

[38] L. Zuo, S.J. Pang, S.F. Zou, H.F. Li, T. Zhang, Surface vitrification of alloys by pulsed electrical discharge treatment, J. Alloys Compd. 707 (2017) 148–154.

[39] M.W. Chen, A brief overview of bulk metallic glasses, NPG Asia Mater. 3 (2011) 82–90.

[40] F.G. Cao, Electro-discharge Machining, first ed., Chemical Industry Press, Beijing, 2014.